Transport, survival and modification of xenoliths and xenocrysts from source to surface

David Sasse[1], Thomas J. Jones[2*] and James K. Russell[1]

Affiliations:
[1] Department of Earth, Ocean & Atmospheric Sciences, University of British Columbia, Vancouver, British Columbia, V6T 1Z4, Canada.
[2] Department of Earth, Ocean and Ecological Sciences, University of Liverpool, Liverpool, L69 3GP, UK.
*Corresponding author: thomas.jones@liverpool.ac.uk

1   **Abstract:** A wide variety of magmas entrain, transport and erupt mantle material in the form of

2   xenoliths and xenocrysts. The host magmas are often low viscosity in nature and range from basalt to

3   more esoteric compositions such as kimberlite, nephelinite and basanite. Here we focus on kimberlite

4   magmas which are particularly successful at transporting deep mantle cargo to the surface, including

5   economically important quantities of diamond. Collections of mantle-derived xenoliths and

6   xenocrysts are critical to our understanding of the structure, stability, composition, thermal state, age,

7   and origin of the lithosphere. However, they also inform on magma transport conditions. Through a

8   series of scaled analogue experiments, we document the relative mechanical stability of olivine,

9   garnet, orthopyroxene, clinopyroxene and diamond xenocrysts during magma ascent. Our experiments

10   fluidized these mantle minerals at a constant gas flux for variable amounts of time approximating

11   transport in a high velocity, turbulent, fluid-rich (supercritical fluid or gas, depending on depth)

12   magma. The evolution of mineral surface features, morphology and grain size distributions is

13   analyzed as a function of residence time. We show that on timescales consistent with magma ascent,

14   each mantle mineral is subject to mechanical modification resulting in mass loss and reshaping

15   (rounding) by grain size reduction and surface pitting. We further discuss the chemical consequences

16   of producing fine particle chips that are highly susceptible to dissolution. Lastly, we utilize an

17   empirical model that relates textural observations (e.g. impact pit size) on xenocrysts to differential

18   particle velocities. Our approach applied to natural kimberlitic olivine and garnet xenocrysts indicates

19   differential velocities of ~ 4 m s^{-1} – the first direct estimate for velocity in an ascending kimberlite

20   magma.

21

22   **1. Introduction**

23   Kimberlites are bodies of volcanic rock preserved at surface as shallow pipes, sheets, dykes

24   and sills across the Earth's cratons (Brown and Valentine, 2013; Dawson, 1971; Russell et al., 2019;

25   Sparks, 2013). Subaerial deposits such as lava and pyroclastic edifices also characterize kimberlite,

26   but are rare due to their poor preservation potential (Brown et al., 2012; Brown and Valentine, 2013).

27   These low viscosity, volatile rich magmas originate deep within the Earth, in excess of 150 km, and

28   are proposed to ascend at anomalously high speeds estimated to be between 1 and 20 m s^{-1} (Eggler,

29   1989; McGetchin et al., 1973; Russell et al., 2012; Sparks et al., 2006; Wilson and Head, 2007).

30   Transit to the surface through the cratonic mantle lithosphere is attended by entrainment of mantle-

31   derived xenoliths and decompression-induced liberation of xenocrysts (Brett et al., 2015); all of which

32   occur on timescales of hours to days (Sparks et al., 2006). The resulting rock, kimberlite, therefore

33   comprises abundant ($\lesssim$ 50% volume; Moss et al., 2010; Smith, 2008) mantle cargo, all encoded with

34   information pertaining to the dynamics of kimberlite transport, ascent and eruption. However, natural

35   samples are often pervasively altered post-emplacement and only limited deposits are fresh enough

36   for quantitative insights to be drawn.

37   Kimberlite magmas ascend in fractures (dykes), facilitated by buoyancy arising from a critical

38   density difference between the magma and surrounding country rock (Russell et al., 2012; Sparks,

39   2013; Sparks et al., 2006). During magma ascent, the overlying mantle is fractured due to over-

40   pressures at the crack-tip, leading to the entrainment of wall rocks as mantle xenoliths (Brett et al.,

41   2015). Fast upward transport subjects xenoliths to rapid depressurization, causing their disaggregation

42   and the subsequent release of xenocrysts into the turbulent, volatile-rich magma (Brett et al., 2015;

43   Jones et al., 2019). Once entrained the mantle xenocrysts may be affected by: (1) chemical dissolution

44   (Arndt et al., 2010; Kamenetsky et al., 2008; Pilbeam et al., 2013) potentially expressed as etch pits

45   and embayments, and (2) mechanical modification (Arndt et al., 2010; Brett et al., 2015; Jones et al.,

46 2019, 2014) by 'attrition' (cf. Jones and Russell, 2018) expressed by grain rounding, breakage and

47 pitting. Textural evidence for these processes is commonly preserved in the properties of kimberlite-

48 hosted xenocrysts. Mechanical modification dominates the surface textures of many mantle

49 xenocrysts within kimberlite, implying that it is particularly important during the later stages of ascent

50 (Arndt et al., 2010; Jones et al., 2019).

51   Previous studies have proposed that beneath the dyke/crack tip there is a low viscosity,

52 volatile-rich region comprising supercritical fluid and/or gas (depending on depth) that turbulently

53 suspends high volume fractions of mantle cargo (Arndt et al., 2010; Brett et al., 2015; Russell et al.,

54 2019). This is followed stratigraphically by a denser, melt-dominated region in the dyke tail (Brett et

55 al., 2015). Mechanical attrition of the mantle cargo within these rapidly ascending (i.e. turbulent)

56 magmas is expressed by reshaping (rounding) and resurfacing of xenoliths and xenocrysts (Arndt et

57 al., 2010, 2006; Barton Jr and Gerya, 2003; Jones et al., 2019, 2014; Kurszlaukis and Barnett, 2003;

58 Peltonen et al., 2002; Peterson and LeCheminant, 1993; Smith and Griffin, 2005). Transport-induced

59 rounding is particularly evident in olivine xenocrysts which volumetrically dominate most

60 kimberlites.

61   Here, we present a series of attrition experiments at scaled conditions relevant to kimberlite

62 ascent for mantle-derived minerals typical of kimberlite cargo (olivine, garnet, orthopyroxene,

63 clinopyroxene, diamond and mixtures thereof). The experiments involve suspending mantle minerals

64 in a turbulent, gas fluidized state for prescribed amounts of time. Our experimental set-up is most

65 relevant to the gas/supercritical fluid-rich (depth dependent) crack-tip environment where ideal

66 conditions are met for sustained and energetic particle-particle interactions supporting attrition (e.g.

67 Brett et al., 2015; Jones et al., 2019). Our experiments inform on the mechanical stability of each

68 mineral and establish quantitative rates of mechanical breakdown (i.e. attrition) for each. We conclude

69 by combining experimental data and observations on natural kimberlite samples to provide

70 quantitative constraints on the timescales and velocities of kimberlite ascent.

71

72 **2. Methods & Materials**

73 **2.1 Characterization of starting materials**

74   Fresh (i.e. unaltered) minerals for this project were sourced from a variety of companies

75   mostly specializing in abrasives or gemstone sales. Forsterite (olivine) sand derived from crushed

76   dunite is from Ashwani Industrial Minerals Corp.; pyrope (garnet) sand is from Zhangjiakou Xuanhua

77   Ju Hong Abrasion Resistant Material Distribution Co., Ltd.; chrome diopside (clinopyroxene) from

78   Sovtube, an unaffiliated seller; and natural rough diamond sand from CDL FINESHINE. The

79   clinopyroxene and orthopyroxene could only be obtained as large (i.e. >5 mm) crystals and were

80   manually crushed using a corundum mortar and pestle. Before using the minerals for experimental

81   purposes, all mineral sands were sieved to the desired, restricted grain size of 600-710 µm and washed

82   using deionized water to remove any adhering fine particles. This size range was selected as it the

83   largest grain size available for all minerals and is therefore the closest to those observed in the natural

84   system. Photographs of representative mineral grains used in the experiments are shown in Figure S1.

85   The density of each mineral was calculated using an analytical balance to measure mass and a

86   Micrometrics Accupyc II 1340 Helium pycnometer to measure volume. Three aliquots of each

87   mineral sample were measured for mass and volume, then plotted as mass [g] against volume [cm^3].

88   A linear regression was then fitted through the three data points and the origin, with the slope

89   determining the density [g cm^{-3}] of the mineral (Table S1). Additionally, a number of grains were

90   imaged using a Philips XL30 scanning electron microscope (SEM) in secondary electron mode with a

91   15-kV accelerating voltage and a 35 µA beam current. Images were taken at various magnifications to

92   document the overall morphology and the surfaces of the starting material prior to experimentation.

93

94

95   **2.2 Attrition Experiments**

96   Experiments were performed at standard laboratory conditions wherein mineral grains (i.e.

97   particles) were suspended in an air-jet. The apparatus (Figure 1) features a compressed air feed that

98   passes through a calibrated FMA 5526 Omega gas flow meter (measuring gas flux, 105 L min^{-1} for all

99   experiments), and into to the base of a 3.5 cm diameter, 120 cm long vertical attrition tube. The gas

100   enters the base of the tube via a distributor plate which features 41 evenly spaced holes (Figure 1). On

101   top of the distributor plate 15 g of input mineral grains (initially 600-710 µm in diameter, termed

102   parent particles) are loaded to an initial bed height, h_0. The distributor plate ensures an equally

103   distributed gas flux, which suspends particles effectively to height, h_p which was measured after the

104   start of each experiment. As particle interactions occur within the attrition tube, fine particles are

105   elutriated from the bed, passing up the attrition tube and into a 70 cm long, 20 cm diameter settling

106   chamber which serves two primary purposes. Firstly, a lower gas flux in the settling chamber allows

107   particles 23-135 μm in diameter to be recycled back into the attrition tube which would otherwise

108   leave the attrition process. Secondly, ultrafine particles (<23 μm) can be elutriated from the settling

109   chamber, passing through an elbow joint, down a tube and into a nylon filter bag (1 μm mesh) where

110   the fines are collected for processing. For each experiment, we recorded the initial bed height (h_0) and

111   the fluidized column height (h_p). Particle concentration (φ) is calculated from values of h_p relative to a

112   model initial dense (pore space free) bed height ($h_{0\,calc}$) as:

$$\varphi = \frac{h_{0\,calc}}{h_p} = \frac{m_0}{\pi r^2 \rho_p h_p} \qquad [1]$$

113   where ρ_p [kg m^{-3}] is the particle density, m_0 [kg] is the input mass is particles and r [m] is the attrition

114   tube radius.

115   The key modifications to this apparatus, relative to the previous work of Jones and Russell

116   (2018) and Jones et al. (2019), is the addition of a settling chamber that allows re-entrainment of

117   particles and the fines collection filter bag which ensures retention of the finest particles whist

118   allowing free flow-through (i.e. no back pressure) of gas. Table S2 (online supplementary

119   information), summarizes the experimental conditions and characterization performed for each

120   experiment in this study.

121
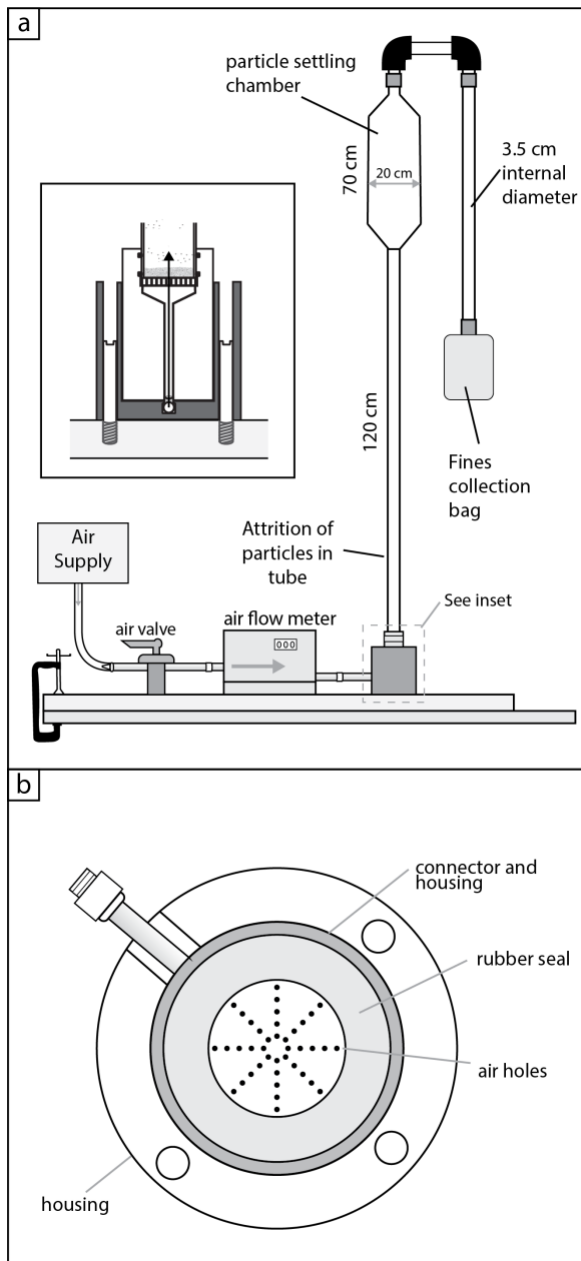
122
123 **Figure 1:** Attrition apparatus used in this study. **(a)** Schematic diagram of apparatus with inset
124 showing sample resting on the distributor plate to be fluidized by the gas jet (solid arrow). **(b)** A plan
125 view of the distributor plate upon which the input sample is loaded.
126

127   We used videography to study and quantify the nature of fluidization and particle interactions.

128 We recorded 20 seconds of select experiments at 1,050 frames per second using a Chronos 1.4 high-

129 speed camera; image collection began ~ two minutes after the gas flux was initiated. To ensure that

130 individual particles could be manually tracked with accuracy, a Godox QT600II high speed flash

131 strobe light was used to illuminate the experiment. For all filming the camera was positioned at a 50

132 cm horizontal distance from the attrition tube. We varied the camera's vertical position between the

133 different mineral experiments to ensure that film captured 50 - 90 % of the total column height. For

134 each mineral type we tracked between 140 and 165 particles over 2-10 frames in a representative

135 experiment. The dataset comprised ~140 particles tracked from the central region of the attrition tube

136 and 30 particles from the margins. This ratio of tracked particles (centre *vs.* margins) is proportional

137 to distribution of particles across the width of the tube; approximately 70% of the tube is occupied by

138 particles moving upward within the central jet and 30% downwelling at the margins.

139

140 **2.3 Post-experiment sample characterization**

141   At the end of a prescribed time, the gas flow was switched off marking the end of the

142 experiment and the apparatus was left for at least 1 hour to ensure fine particles had settled. At that

143 point, the attrition apparatus was carefully disassembled and washed with deionized water over a

144 standard stack of ASTM E11 mechanical sieves with a mesh size range of 125 µm to 600 µm and a

145 collection pan below the 125 µm sieve. The sieves were then left to dry in a 70°C oven overnight. The

146 following day the material was dry sieved and the contents of each sieve were weighed using an

147 analytical balance ($\pm$ 0.1 mg). All material collected below the input parent size (600 – 710 µm)

148 represents particle sizes derived from the attrition process, which we term 'daughter' particles' herein.

149 Grain size distributions of material caught in the pan (i.e. <125 µm) were measured by Laser Particle

150 Size Analysis (LPSA). A Malvern Mastersizer 2000 laser diffraction device with a hydro 2000 Mu

151 water dispersion module attached was used for LPSA in this study. The pump speed, absorption

152 coefficient and refractive index were varied for each mineral (see Table S3). Each aliquot of sample

153 added to the dispersion module was measured three times. To prevent particle aggregation, an

154 ultrasonic pulse was applied for 2 seconds immediately before measurement. This process was

155 repeated three times for a total of nine measurements. To obtain the final particle size distribution of

156 the powder, the nine measurements were averaged for a mean grain size distribution. The

157 experimental run products were also characterized for morphology and surface features using the

158 SEM as reported above (cf. Section 2.1).

159

160 **3. Results and Analysis**

161   Our experimental campaign consisted of a total of 43 experiments that fluidized an initial

162   mass (m_0) of 15 g of one of the minerals olivine, garnet, clinopyroxene, orthopyroxene, or diamond

163   with a gas flux of 105 L min^{-1}.

3.1 Experimental Observations

165   Throughout all experiments, particles were distributed throughout the column and able to

166   move freely relative to neighboring particles indicating a pneumatic flow regime (Bi and Grace, 1995;

167   Jones et al., 2019). As would be expected, column height and the particle's density are negatively

168   correlated whereas particle concentration and particle density are positively correlated. Specifically, at

169   fixed gas flux (105 L min^{-1}), orthopyroxene had the largest mean column height of 218.0 ± 2.7,

170   followed by olivine, clinopyroxene, diamond and garnet with h_p values of 209.4 ± 5.3 mm, 209.3 ±

171   3.9, 189.3 ± 3.5 and 172.3 ± 3.4 mm respectively. This resulted in similar average particle

172   concentrations of, 0.02214 ± 0.00028, 0.02295 ± 0.00058, 0.02265± 0.00043, 0.02348 ± 0.00043 and

173   0.02327 ± 0.00047 (cf. Table S4).

174   Particle motion within the tube is not entirely random, the central region of the tube is

175   dominated by an upward stream of relatively fast-moving particles, which contrasts the slower,

176   predominantly downward, particle motion at the tube margins. The particle tracking results for each

177   mineral are visualized in Figure 2. The histogram plots for each mineral show a bimodal distribution

178   with one mode at a positive velocity and another mode at a negative velocity. The differential velocity

179   (Δv) is approximated by taking the difference between the two velocity modes. This is 1.0 m s^{-1} for all

180   experiments apart from orthopyroxene and diamond, where $\Delta v = 1.25$ m s^{-1} and 0.75 m s^{-1},

181   respectively. The velocity contours for each mineral show a central jet characterized by relatively

182   large, positive velocities ('hot' colors) and negative velocities ('cold' colors) at the margins of the

183   tube.
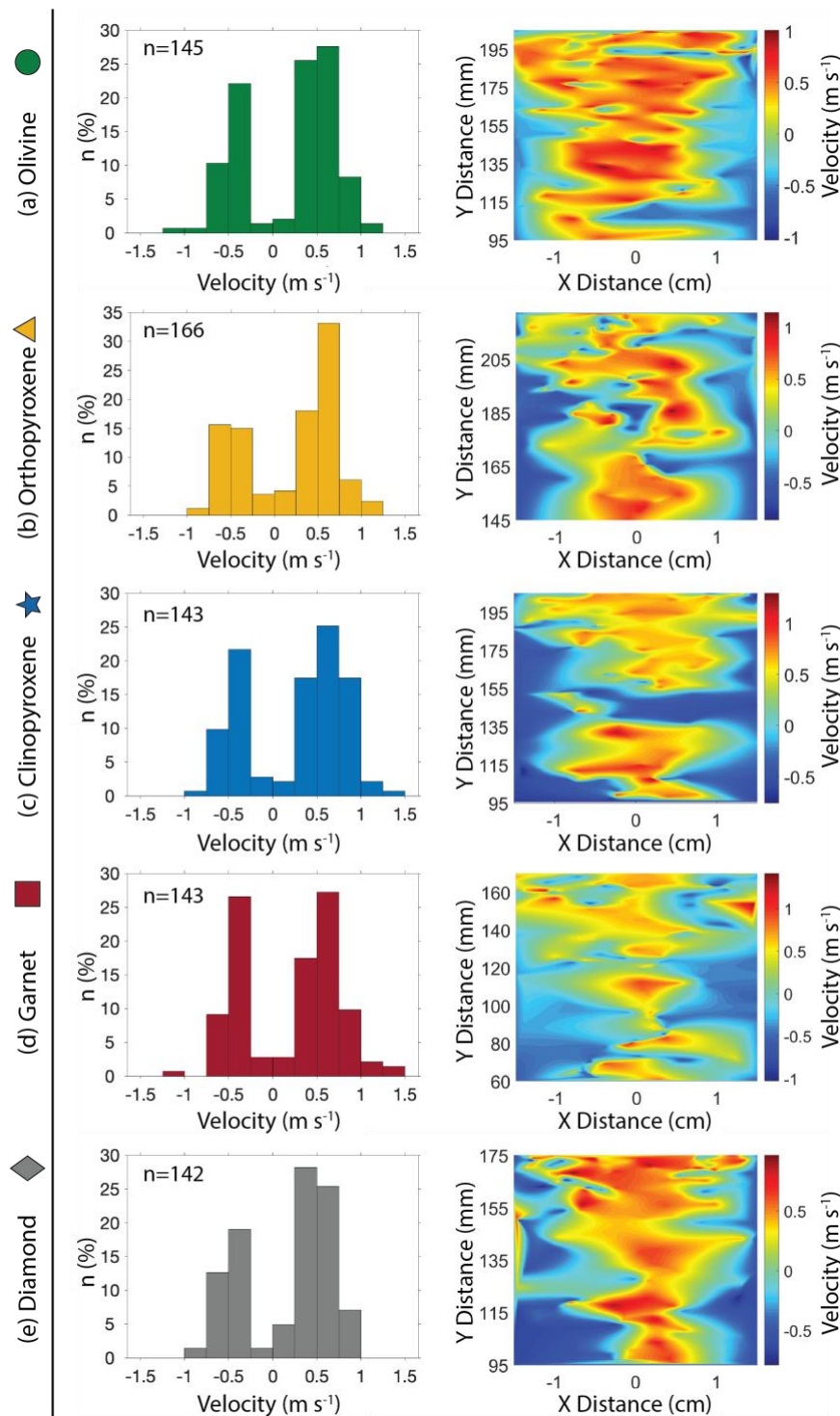
Figure 2: Particle tracking results for a) olivine, b) orthopyroxene, c) clinopyroxene, d) garnet, e) diamond. Left column: velocity values plotted as histograms with a 0.25 m s⁻¹ bin width. Right column: velocity distributions within the attrition tube where Y is the distance above the base of the tube and X is the distance across the tube. Accompanying videos can be found in the online supporting information and are labelled S1 through S5 corresponding to the panels (a) through (e) respectively.

3.2 Fines production datasets and models

193   The production of daughter particles serves as an effective and simple measure to quantify the

194   attrition process (Gwyn, 1969). The mass of daughter particles (m_d) relative to the total mass

195   recovered (m_r), as a function of time t [h] for each mineral is shown in Figure 3. Each suite of

196   experiments shows an initial, rapid rise in the production of daughter particles followed by a highly

197   reduced rate ultimately forming a plateau and indicating little further attrition. In the literature this

198   plateau is recognized as a stable state where production of daughter particles becomes limited with

199   increased residence time (Jones et al., 2017; Knight et al., 2014). The time-dependent trends are well

200   modelled by the empirical function:

$$\frac{m_d}{m_r} = a(1 - e^{-bt}) \qquad [2]$$

201   (Jones et al., 2017). The two adjustable parameters, a and b, represent the infinite time attrition limit

202   (i.e. the plateau) and the attrition rate constant [h^{-1}] dictating the rate (i.e. initial slope) at which that

203   limit is reached, respectively.
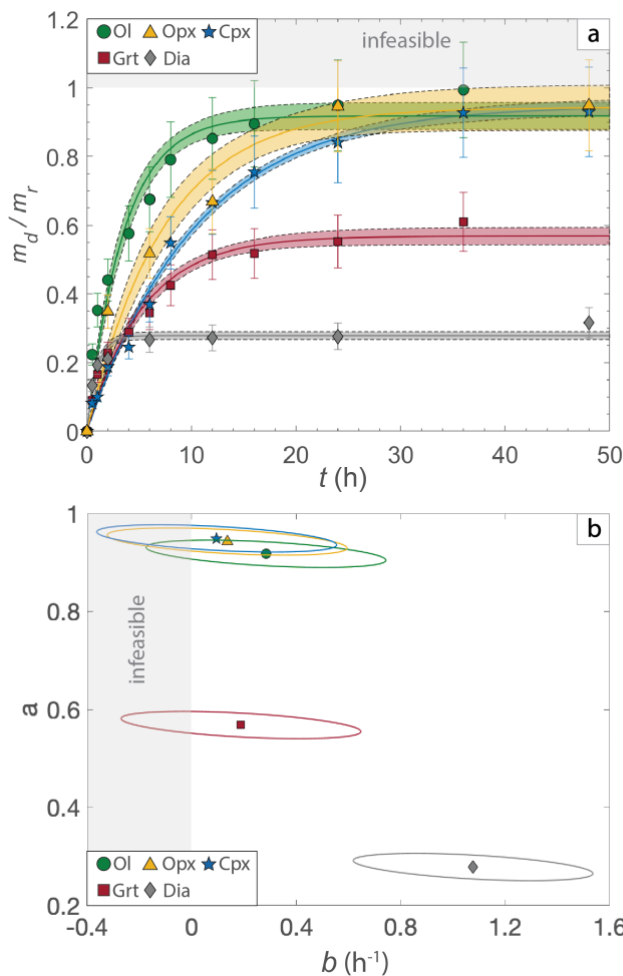
204

205 **Figure 3: (a)** Proportion of daughter products (m_d) normalized to the mass recovered (m_r) plotted
206 against time for each mineral series. Error bars represent two relative standard deviations obtained
207 from repeating experiment 1-F three times. Dashed lines bounding the coloured region for each
208 mineral series are 95% confidence limits for the optimal fit (solid line). The accompanying mass loss
209 data can be found in Table S5. **(b)** Model values of *a*, the infinite time limit of attrition and *b*, the
210 attrition rate constant for all minerals. The ellipses represent 95% confidence envelopes on the
211 optimal solution (i.e. *a* and *b*; Eq. 2). See Table 1 for fit parameters.
212
213

| Mineral	*a*	*b* (h^{-1})	RMSE of fit
Olivine	0.9179	0.2840	0.0708
Orthopyroxene	0.9427	0.1355	0.0793
Clinopyroxene	0.9492	0.0955	0.0312
Garnet	0.5682	0.1884	0.0381
Diamond	0.2784	1.0770	0.0231

214 **Table 1:** Modelled fit parameters for Eq.2 for each mineral series. RMSE = Root Mean Square Error.
215

216   The model functions (Equation 2; Table 1) describe the experiment data well and the 95%

217 confidence limits establish the range of *a* and *b* values that are consistent with the individual datasets

218 and their measurement uncertainties (Figure 3). We distinguish two groups of minerals that form

219 similar shaped trends (1) olivine, garnet and diamond; (2) clinopyroxene and orthopyroxene. For set

220 (1), the attrition plateau is reached within 16 hours, but minerals are characterized by different

221 attrition limits (*a*) and rates (*b*). Specifically, olivine has the highest *a* value of 0.9179 followed by

222 garnet and diamond with values of 0.5682 and 0.2784 respectively. Diamond approaches its attrition

223 limit the fastest followed by olivine and garnet. For set (2), the two pyroxene minerals, orthopyroxene

224 and clinopyroxene, the attrition limit (i.e. *a*) is only just met within the experimental timescale, but

225 this attrition limit is similar to olivine at the 95% confidence limits. The largest difference between

226 sets (1) and (2) is in the rate at which the attrition limit is approached (*b*); the pyroxenes have slower

227 rates (0.1355 h^{-1} and 0.09554 h^{-1}) relative to olivine (0.2840 h^{-1}).

228

229 **3.3 Total grain-size distributions**

230 The experiments show a characteristic rapid initial drop in abundance of the parent grain population

231 (grey mode; Figure 4) over short times. This decrease in the parent population is accompanied by the

232 development of secondary grain-size modes representing the daughter products resulting from

233 attrition. Interestingly, the grain size distributions for each mineral type feature a number of modes

234   and mode positions unique to that mineral. These characteristic distributions directly reflect the

235   physical properties of each mineral.

236
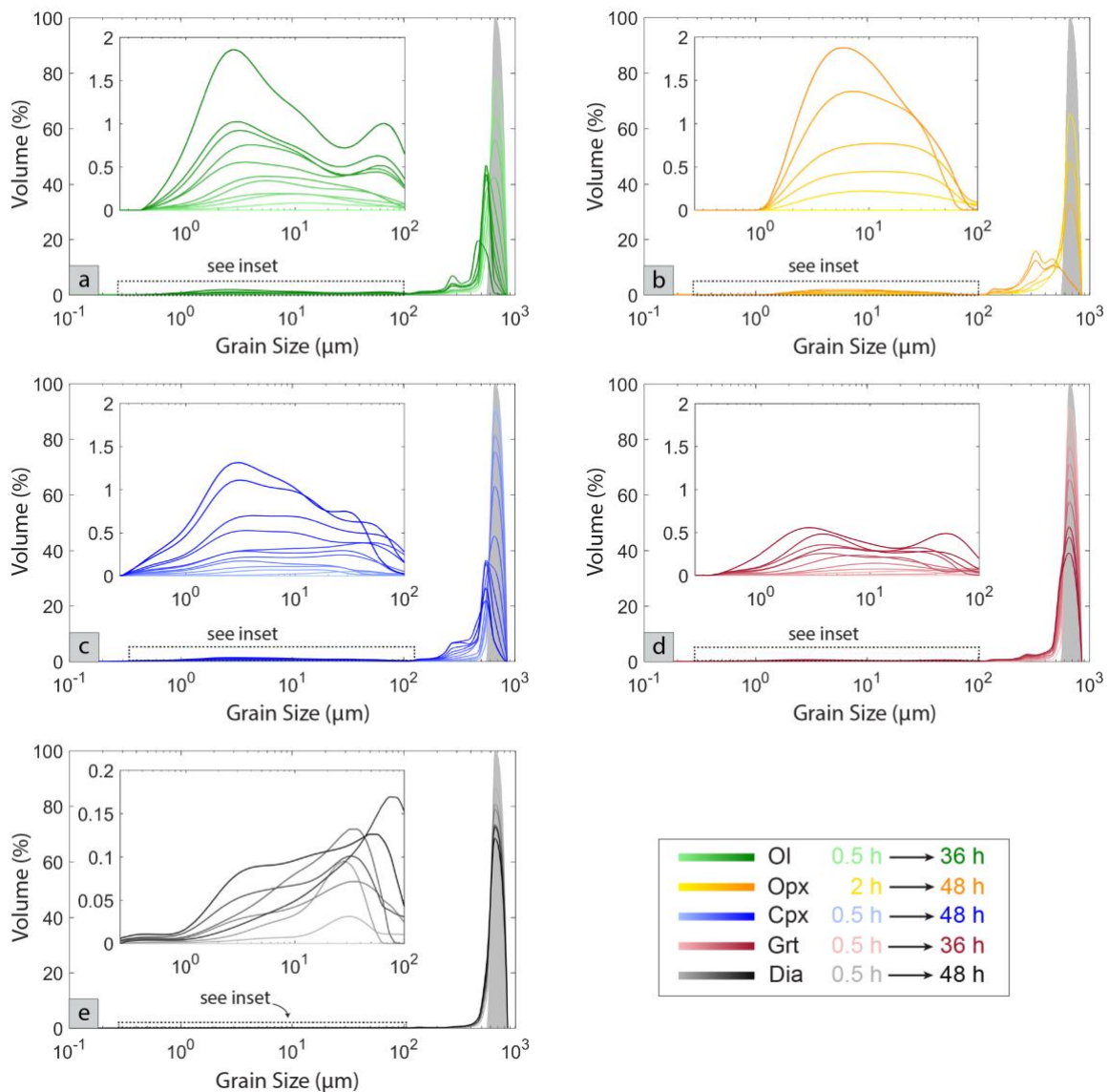
Figure 4: Grain size distributions for each mineral series: **(a)** olivine; **(b)** orthopyroxene; **(c)**
clinopyroxene; **(d)** garnet; **(e)** diamond. The input distribution is shaded in grey and presents the
initial parent mode that evolves with time. The experiment run products are plotted as continuous
lines which become darker with increasing experiment duration (see legend). Experiment durations
for each mineral series are shown in Table S2. Insets show the finer daughter products measured by
laser particle size analysis (LPSA), at an enlarged scale. For the reader's ease the diamond inset y-axis
scale is an order of magnitude lower than the other plots to account for the low abundances of
diamond daughter products.

245

246   The parent mode for olivine (Figure 4a) decreases from 655 µm to 500 µm with increased

247   residence time up to 6 h. At the longest duration (36 h), the mode position changes again to ~ 463 µm.

248   After 6 h a secondary daughter mode at 275 µm begins to form. Two finer modes below 100 µm at 3

249   μm and 65 μm exist (see inset) for a total of four modes. Orthopyroxene shows an initial rapid decline

250   in the parent mode which moves towards a position of 463 μm at 24 h. At 24 h a secondary mode at

251   328 μm becomes very noticeable (Figure 4b). Unlike the other minerals, orthopyroxene below 100

252   μm is characterized by a broad unimodal distribution centered on 6 μm for a total of three modes.

253   Another peak may occur at 26 μm but is obscured by the breadth of the distribution. Clinopyroxene

254   shows a parent population that shifts towards a peak position of 500 μm with increased residence time

255   (Figure 4c). Development of a secondary mode at 275 μm is evident after 24 h. At long times (> 24 h)

256   the parent mode broadens and is skewed to the finer grain sizes indicating possible emergence of

257   another mode at 463 μm. Below 100 μm, two modes are identified, one at 3 μm and another at 31μm.

258   The latter migrates towards 48 μm at long times (> 16 h). A total of four modes are identified for

259   clinopyroxene. Garnet shows a declining parent peak which, unlike the other minerals, does not

260   change grain-size position (Figure 4d). A secondary mode is observed at 275 μm starting at 16 h.

261   Below 100 μm there exists a bimodal fines population with modes at 3 μm and 52 μm for a total of

262   four modes. Lastly, diamond shows far less attrition than the other minerals. This is indicated by a

263   persistent parent mode which, as seen in garnet, does not shift towards a smaller mode (Figure 4e). No

264   secondary mode is observed and a relatively low volume of fines (<100 μm) is produced (note that the

265   inset volume % scale has been lowered by an order of magnitude). Below 100 μm a bimodal

266   population is observed, with one peak at 4 μm and another at 31μm shifting towards 78 μm at longer

267   (24 h) residence times. A total of three modes are observed for diamond.

268

269   **3.4 Xenocryst morphologies and surfaces**

270   Initially all mineral grains have angular morphologies, sharp edges and smooth surfaces.

271   Grains of pyroxene start with slightly higher aspect ratios (long axis: short axis) due to their inherent

272   cleavage. With increased residence times all parent mineral grains transition towards rounded

273   morphologies with micro-rough surfaces (Figure 5). In general, morphological changes to the parent

274   particles are most profound in the first two hours of attrition, where particles rapidly lose asperities

275   and the overall morphologies round. Further changes in particle shape slow as residence time

276   increases.

277   Olivine undergoes the most efficient modification expressed by highly rounded grain

278   morphologies and rough surfaces. Orthopyroxene and clinopyroxene show distinct cleavage-

279   controlled disruption with planar breakage surfaces resulting in high aspect ratio products (Figure 5).

280   These higher aspect ratios might make pyroxenes more susceptible to further attrition. Garnet shows

281   conchoidal fracture and a morphology similar to olivine after long ($\geq$ 12 h) residence times. Both

282   minerals evolve to aspect ratios close to 1, however, garnet grain surfaces sometimes show less pitting

283   relative to olivine. The diamond input particles (i.e. 0 h) show perfectly straight and sharp edges and

284   flawless surfaces controlled by the perfect cleavage. The rounding and surface modification of

285   diamond is much less than the other minerals, yet they still round and become pitted.

286   Higher magnification images of milled grains (Figure 5) show a range of surface features

287   from small scale (<20 μm) surface depressions resulting from lower energy, more frequent collisions

288   to larger scale (>100 μm) impact features resulting from higher energy collisions. The nature of the

289   impact features varies by mineral type and, to an extent, is controlled by cleavage. Olivine and garnet

290   have impact depressions and excavations that are hemispherical in shape, have a smooth interior

291   surface, and are randomly oriented. By contrast, orthopyroxene, clinopyroxene and diamond show a

292   higher degree of flaking and layering with impact pits appearing more elongated. Flaking at, and

293   beneath, the exterior surface is not restricted to cleavage and is also observed, although less

294   frequently, in both olivine and garnet. Other authors have identified these subsurface textures and

295   flaky surfaces as a stress release mechanism in response to either decompression or heating (Campbell

296   et al., 2013; Jones et al., 2014; Little et al., 2017). Furthermore, subsurface layering/flaking has also

297   been documented in natural diamonds and interpreted as brittle fracturing during both magma

298   transport and post emplacement (Win et al., 2001).
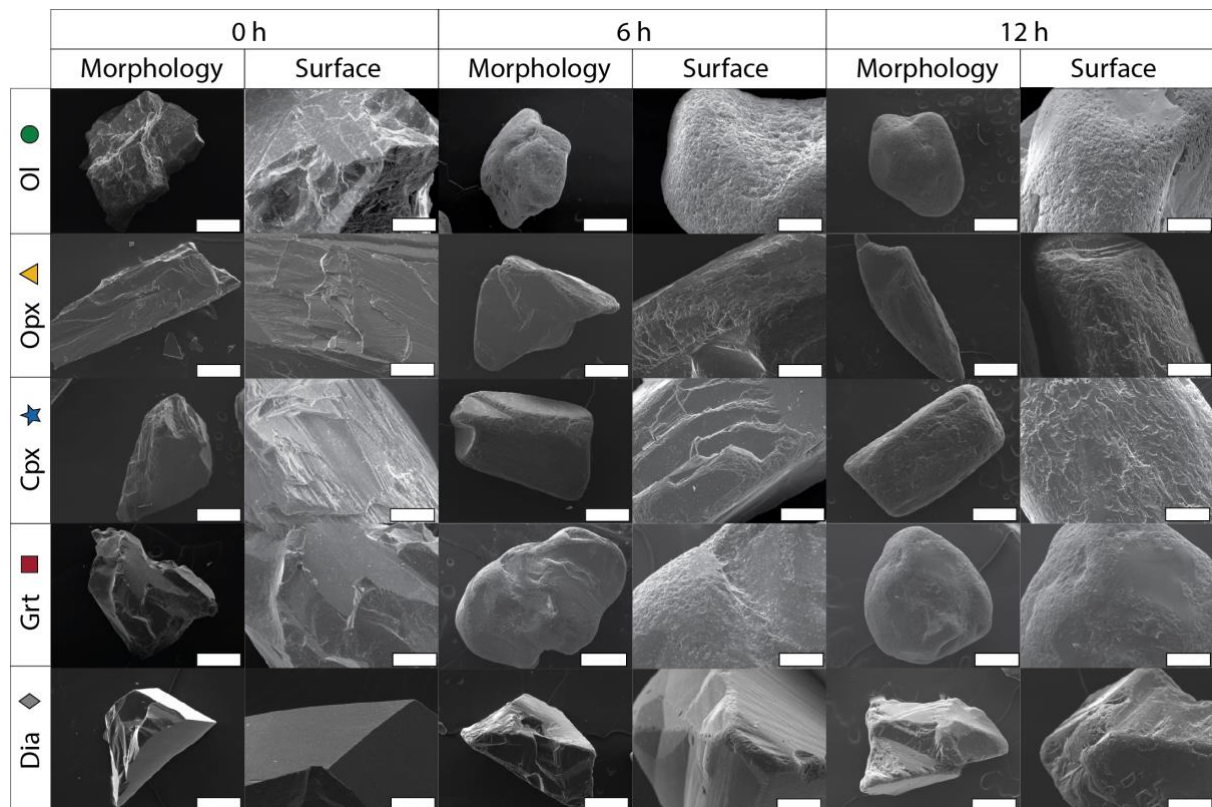
299
300 **Figure 5:** SEM images (in secondary electron mode) of representative parent particle morphology and
301 surface features at select experiment durations. Rows represent different minerals and columns denote
302 experiment duration. White scale bars denote 300 µm for the morphology images and 100 µm for the
303 surface images. Further imagery can be found in Figure S2.
304

305

306 **4. Discussion**

307 **4.1 Relating experiments to nature**
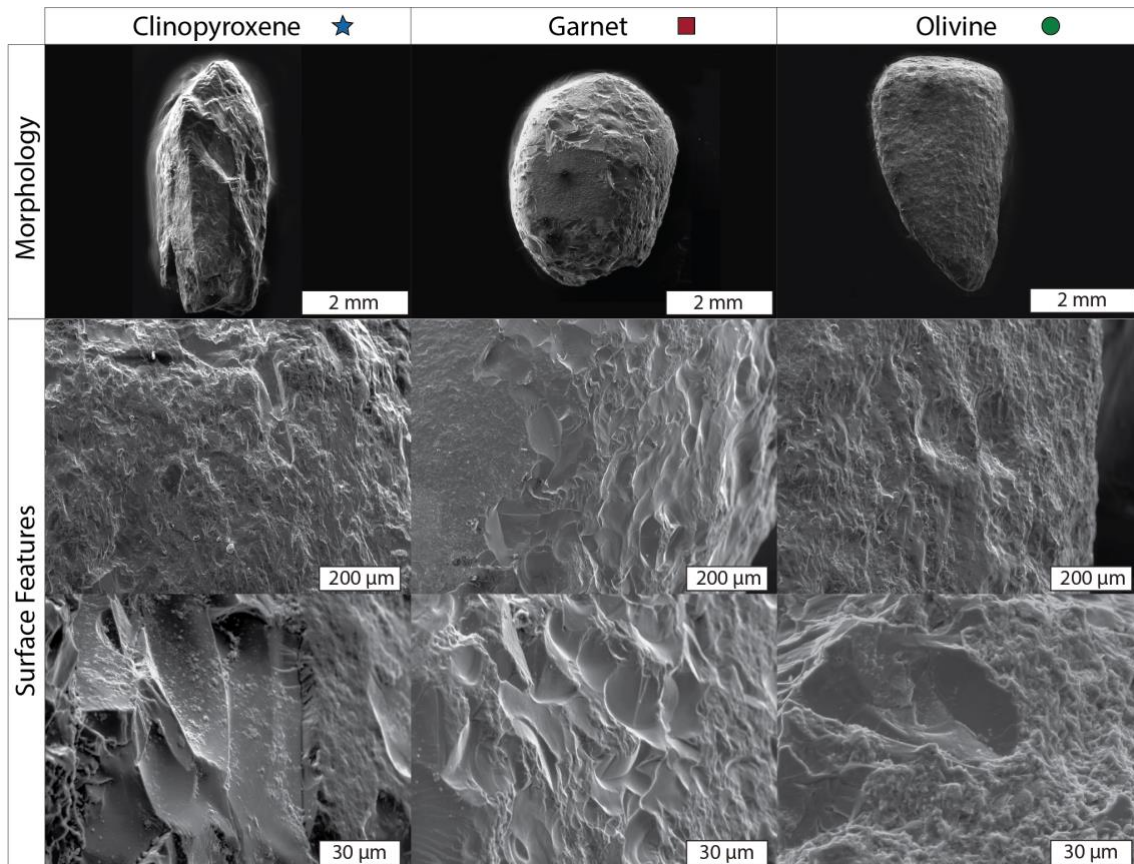
308
309 **Figure 6:** Scanning electron microscope images of the morphology and surface features of xenocrysts
310 from Diavik A154N coherent kimberlite taken in secondary electron mode. Top row shows rounded
311 shapes of clinopyroxene, garnet and olivine mineral grains. Surfaces of these minerals are rough
312 (middle row) and, in detail, are micro-chipped and flaked (bottom row).
313

314   To compare the products of our experiments to natural samples, xenocrysts were analysed

315 from the Diavik kimberlite deposit located in the Northwest Territories, Canada, part of an economic

316 ore body within the Lac de Gras kimberlite field. Specifically, clinopyroxene, garnet and olivine

317 grains from coherent kimberlite of the A154N pipe (~650 m drill depth) were carefully extracted and

318 imaged under the SEM (Figure 6). First, we used a diamond drill tip to extract an area of groundmass

319 encasing the grain. Then the grains were carefully rinsed under water to remove the attached

320 groundmass.

321   Images of xenocrysts recovered from natural samples of kimberlite show a remarkable

322 resemblance to the experiment products (Figure 6 *vs.* 5). The kimberlitic xenocrysts display rounded

323 morphologies and rough surfaces dominated by impact pits. The creation of surface textures in

324 kimberlite can broadly be divided into 'chemical' and 'mechanical' processes (Jones et al., 2019,

325 2014). Chemical textures can originate from either magmatic melt and/or fluid dissolution or

326   crystallization (Fedortchouk, 2019; Giuliani, 2018; Kamenetsky et al., 2008; Pilbeam et al., 2013)

327   whereas mechanical textures originate from attrition driven by particle-particle collisions (Arndt et al.,

328   2010, 2006; Brett et al., 2015; Jones et al., 2019, 2014; Jones and Russell, 2018). A comparison of

329   features resulting from these contrasting modes of surface modification are illustrated in Figure S3.

330   Cavities formed by chemical etching appear strongly controlled by crystallography, having sharp

331   edges and regular geometry (Figure S3). In contrast, impact pits have convex outlines and

332   hemispherical morphologies (Figure S3). Importantly the surface features observed on natural

333   kimberlite xenocrysts (Figure 6 and S3) are dominantly mechanical in nature and thus, at a minimum,

334   mechanical processes dominate during the final stages (i.e. < 100 km) of ascent (Arndt et al., 2010;

335   Brett et al., 2015; Jones et al., 2019, 2014; Jones and Russell, 2018).

336   Mechanical modification, or attrition, creates new grain size populations and surface textures

337   by both fragmentation and abrasion (e.g. Bemrose and Bridgwater, 1987). Fragmentation is a high-

338   energy process resulting in wholesale breakage of the parent particles often producing a small number

339   of similarly sized daughter particles (e.g. Dufek et al., 2012; Jones et al., 2017; Jones and Russell,

340   2017; King, 2001). Sometimes fragmentation can occur through the incremental breakage of particles

341   as expressed in the olivine experiments by the appearance of a secondary daughter mode at 275 µm

342   after 6 h (Bonfils et al., 2016). Abrasion is a lower energy process generating a large number of small

343   chips through the rounding of parent particles (e.g. Jones et al., 2016; King, 2001; Kueppers et al.,

344   2012; Manga et al., 2011). Fragmentation processes operating on kimberlite xenocrysts have been

345   discussed in detail by Jones et al. (2019). They showed that fragmentation occurs at, or above, a

346   critical impact velocity. For olivine, garnet and diamond parent particles the critical fragmentation

347   velocities are 0.54, 0.96 and 1.2 m s^{-1} respectively.

348   The average differential velocities (i.e. impact velocity) in each experiment are ~1.0 m s^{-1}

349   supporting fragmentation of olivine and garnet, whereas fragmentation of diamond should be rare or

350   unlikely. This is in excellent agreement with our grain size distributions (Figure 4) which showed an

351   intermediate daughter (fragmentation) mode for both olivine and garnet, but not for diamond. A lack

352   of literature values for fracture surface energies for diopside and enstatite precluded calculation of

353   their critical fragmentation velocities (Table S1). However, their relatively weak physical properties

354   (Table S1) imply that the intermediate peaks observed in the grain size distributions result from

355   fragmentation. Abrasion processes will be discussed further in Section 4.3.

356   When ascending in a multiphase mixture (i.e. not monomineralic), we hypothesize that the

357   minerals with cleavage, most importantly orthopyroxene, will experience a relatively higher rate of

358   attrition. The high surface area to volume ratios of these fine-grained attrition products of

359   orthopyroxene (Figure 5) would be particularly susceptible to chemical assimilation by the melt

360   (Mitchell, 1986; Mitchell et al., 2019) thereby changing melt composition, decreasing CO_2 solubility

361   and increasing the potential for assimilation fueled buoyant ascent driven by CO_2 fluid exsolution

362   (e.g. Russell et al., 2012; 2019). This creates a positive feedback cycle in which CO_2 exsolution

363   increases magma ascent velocity, leading to more breakage and assimilation, continually supporting

364   turbulent ascent. A corollary of assimilation is that a limited record of attrition processes, particularly

365   the production of daughter fragments, will be preserved in the deposits.

366

367   **4.2 Transport duration and velocity of kimberlite ascent**

368   Kimberlite magmas have been ascribed higher than average ascent rates relative to other

369   mafic magmas (e.g. Eggler, 1989; Sparks et al., 2006; Wilson and Head, 2007; Russell et al., 2012).

370   The rapid ascent (10's of m s^{-1}) of kimberlite is a concept that has been investigated by many authors

371   (Brett et al., 2015; Eggler, 1989; Jones et al., 2019, 2014; Jones and Russell, 2018; Kavanagh and

372   Sparks, 2009; McGetchin et al., 1973; Russell et al., 2019, 2012; Sparks et al., 2006; Sparks, 2013;

373   Wilson and Head, 2007). However, the dynamics remain a highly debated topic. Specifically, the

374   timescales and velocities associated with magma ascent are poorly constrained; velocity estimates

375   range from 1-20 m s^{-1} (Sparks et al., 2006; Wilson and Head, 2007) resulting in transport timescales

376   of days to hours.

377   Our experiments are shown to be correctly scaled for the natural system, in that, they fall

378   within the same dynamical regime (e.g. turbulent flow) and dimensionless space best estimated for

379   kimberlite magmas. Flow regimes are quantified by using the Reynolds number (Re) and specifically

380   for kimberlite (Re$_k$) is expressed as:

$$\mathrm{Re}_k = \frac{Dv\rho}{\mu} \qquad [3]$$

381   where D [m] is the dyke width, v [m s^{-1}] is the velocity of the ascending magma, ρ [kg m^{-3}] is the bulk

382   density and μ [Pa s] is the bulk viscosity of the three-phase fluidized mixture (melt, crystals,

383   volatiles). The associated range of values of Re$_k$ for kimberlite is $\sim 10^2 - 10^6$ (see Table S6).

384   Similarly, the Reynolds number of the flow in our experiments (Re$_{exp}$) is given by:

$$\mathrm{Re}_{exp} = \frac{Lv^*\rho^*}{\mu^*} \qquad [4]$$

385   where L is the attrition tube internal diameter [m], v^* [m s^{-1}] is the bulk velocity [m s^{-1}], ρ^* is the bulk

386   density [kg m^{-3}] and μ^* [Pa s] is the bulk viscosity. We adopt a mixture-based approach (Weit et al.,

387   2018) for calculation of bulk (denoted by the * superscript) velocity, density and viscosity of the

388   fluidized mixture of gas and particles. The bulk velocity (v^*) is given by:

$$v^* = \varphi v_p + (1 - \varphi)v_g \qquad [5]$$

389   where φ is the particle concentration, v_p [m s^{-1}] is the average absolute particle velocity, recorded by

390   high-speed videography and v_g [m s^{-1}] is the superficial gas velocity. The bulk density (solid + gas) of

391   the mixture (ρ^*) is given by:

$$\rho^* = \varphi\rho_p + (1 - \varphi)\rho_g \qquad [6]$$

392   where ρ_p [kg m^{-3}] is the particle density and ρ_g [kg m^{-3}] is the gas density. Lastly, the bulk viscosity

393   (μ^*) of the two-phase mixture is given by (Mader et al., 2013):

$$\mu^* = \mu_g(1 + \frac{5}{2}\varphi) \qquad [7]$$

394   where μ_g [Pa s] is the gas viscosity. The parameters (i.e. φ, ρ_p, v_p) vary for experiments using different

395   minerals and, thus, Re$_{exp}$ will vary slightly. For each mineral the calculated values of Re$_{exp}$ are well

396   within the range of Re$_k$ values expected for kimberlite transport (i.e. $\sim 10^2 - 10^6$): olivine (2.46×10^5),

397   orthopyroxene (2.37×10^5), clinopyroxene (2.47×10^5), garnet (2.98×10^5), and diamond ($2.71 \times$

398   10^5).

399   Equating Re$_k$ and Re$_{exp}$ for each mineral experiment series and rearranging yields the velocity

400   of the kimberlite magma: $v = \mathrm{Re}_{exp}\mu/\rho D$. For example, a 1.5 m wide dyke containing a magma

401   with bulk density (ρ) of 2100 kg m^{-3} and a viscosity (μ) of 0.05 Pa s suggests corresponding velocities

402   for the olivine, orthopyroxene, clinopyroxene, garnet and diamond experiments of 3.91, 3.77, 3.91,

403   4.74 and 4.31 m s^{-1}, respectively. To relate the model attrition rates (cf. Figure 3) to kimberlite ascent,

404   the time axis is converted to distance using the characteristic velocities estimated above (Figure 7).

405   The resulting curves now show attrition-related mass loss as a function of transport distance once the

406   kimberlite magma is in a fluidized, turbulent state. We note that the exact distances will vary upon

407   changing the assumed kimberlite dyke width, density and viscosity, however broad insights can be

408   drawn.

409   At the transport conditions described above, all minerals, except diamond, suffer continual

410   mass loss over 200 km of transport (Fig. 7a). Over this distance olivine shows the largest magnitude

411   of mass loss and therefore serves as the best mineral to document the transport distance in a vigorous,

412   turbulent state. Milling of olivine is highly sensitive to transport distance relative to the other mantle

413   minerals investigated especially over short (< 50 km) distances, thus is the best mineral to resolve

414   short transport distances (Fig. 7b). Diamond reaches the plateau faster than all other minerals mainly

415   because, after ~30 km of transport, diamond ceases to break down at a measurable rate. The

416   mechanical modification of diamond, therefore, can only be used to discriminate between short ($\lesssim$ 30

417   km) and long $\gtrsim$ 30 km) transport distances. These mass loss relationships are also dependent on the

418   gas flux and mass input used in the experiments (Jones et al., 2019). This means that in application of

419   these models to the ascending kimberlite dyke, the choice of particle concentrations and energy

420   (velocity) needs to be chosen with caution.
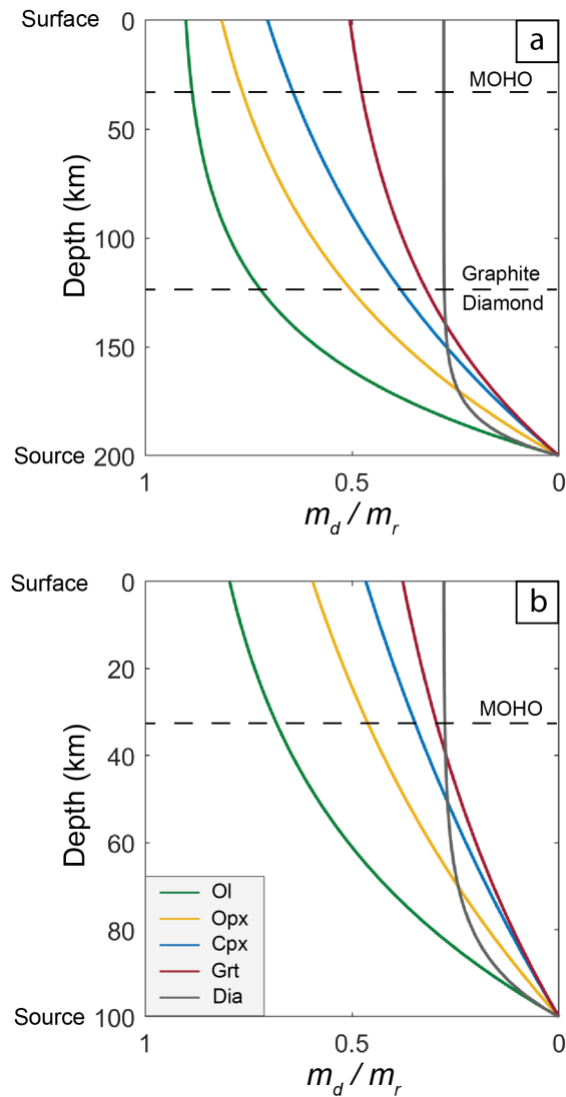
Figure 7: Mineral series attrition curves where the x-axis is converted to distance using calculated ascent velocities. **(a)** Vigorous, high Re ascent (onset of attrition) begins at the source depth of 200 km. **(b)** Fluidization begins at a depth of 100 km. The Mohorovičić discontinuity (MOHO) and the top of the diamond window have been marked for reference.

4.3 Impact pits on xenocrysts record transport velocities

Surface textures on xenoliths and xenocrysts (e.g., impact pits, striae, flaking) entrained by

low viscosity magmas have been long been recognised as hallmarks of abrasion processes (Arndt et

al., 2010; Jones et al., 2014; Jones and Russell, 2018; Kurszlaukis and Barnett, 2003; Peltonen et al.,

2002). These mechanical processes are thought to occur at the volatile-rich dyke head under turbulent

flow conditions (e.g., Brett et al., 2015) – the same conditions that our experiments are scaled for

(Figure 8a). Here we use surface features on natural and experimental xenocrysts, especially the

434   impact pits, to characterize the environment and to quantify internal velocities within the magma-

435   filled dyke during transport (Figure 8a).

436   Abrasion is a localized stress release mechanism and can be divided into surface wear and

437   chipping (Boerefijn et al., 2007; Ghadiri and Zhang, 2002). Surface wear takes place at the micron

438   scale, releasing ultra-fine particles and is associated with plastic deformation and shear stress at the

439   surface of the grain (Hutchings, 1993). In the case of chipping, a fracture propagates from the site of

440   impact, extending laterally and curving to towards the surface (Ghadiri and Zhang, 2002). This

441   produces chips, often larger in size than those produced by surface wear. Our abrasion products

442   typically show a bimodal distribution (insets; Figure 4), in which the coarser mode is produced by

443   chipping exclusively and the finer mode can be produced by both chipping and surface wear, although

444   likely dominated by the latter.

445   Surface abrasive wear of materials is commonly linked to hardness (Archard, 1953;

446   Hutchings, 1993). The model proposed by Archard (1953) relates the extent of breakage by surface

447   wear (ζ_{wear}) to the normal compressive force acting on the particle (F [mN]), the sliding distance (Δs

448   [m]) and the material hardness (H [Pa]):

$$\zeta_{wear} = \alpha_w \frac{F\Delta s}{H} \qquad [8]$$

449   where α_w [m^{-3}] is a material-dependent proportionality factor. In kimberlite magmas, we would expect

450   the harder minerals (e.g., diamond) to be less prone to surface wear relative to, for example, olivine

451   (Table S1). The extent of breakage by chipping (ζ_{chip}) has been described by Zhang and Ghadiri

452   (2002):

$$\zeta_{chip} = \alpha_c \frac{H}{K_c{}^2} \rho_p v_i{}^2 d_p \qquad [9]$$

453   where K_c [Pa m$^{-0.5}$] is the fracture toughness, ρ_p [kg m^{-3}] is the particle density, v_i [m s^{-1}] the impact

454   velocity and d_p [µm] is the particle diameter. The variable α_c [kg m$^{-0.5}$ s^2] is a material-dependent

455   proportionality factor. The relationship is strongly dependent on the brittleness factor (Ghadiri and

456   Zhang, 2002; Zhang and Ghadiri, 2002), a ratio of the hardness to the fracture toughness ($H K_c{}^{-2}$).

457   This implies that, in kimberlite, more brittle materials (e.g. diamond, garnet; Table S1) are more prone

458   to chipping. Equations 8 and 9 explain the relative peak sizes (cf. Figure 4) of the abrasion products

459   (<100 µm). Surface wear is limited to the finer mode (< 20 µm) and chipping contributes to both the

460   coarser mode (80 – 100 µm) and the finer mode.

461   Impact pit geometries produced by chipping have been related to the impact velocity (Ghadiri

462   and Zhang, 2002; Zhang and Ghadiri, 2002):

$$i = klv_i^{\frac{1}{2}}\left(\frac{\rho_p}{H}\right)^{1/4} \qquad [10]$$

463   where i [m] is the impact pit diameter, k is a proportionality constant and l [m] is the particle diameter.

464   Equation 10 assumes hemispherical impact geometry and an equant particle morphology. In natural

465   kimberlite xenocrysts and in our experimental run products, surfaces of olivine and garnet grains

466   exhibit hemispherical impact pits (cf. Jones et al., 2014). Twenty pit-diameters were measured on

467   both olivine and garnet grains collected from short (2h), intermediate (12h) and long duration (36h)

468   experiments yielding a total of 60 measurements per mineral (Table S7). These pit measurements

469   were then used in conjunction with our well-constrained experimental data, $v_i = 1$ m s^{-1} (differential

470   particle velocities; Fig. 3) and modal grain sizes from Fig. 4 to fit for the corresponding

471   proportionality constants (k) for olivine and garnet: 0.62 ($1\sigma = 0.170$) and 0.46 ($1\sigma = 0.117$),

472   respectively.

473   Equation 10 can be rearranged to solve for impact velocity from measurements of impact pits

474   on natural kimberlite xenocrysts using our experimentally derived proportionality constants:

$$v_i = \left(\frac{i}{kl\left(\frac{\rho_p}{H}\right)^{1/4}}\right)^2 \qquad [11]$$

475   This provides a valuable quantitative tool to directly relate textures observed on natural kimberlite

476   xenocrysts to their differential velocities within the ascending magma. Furthermore, our approach is

477   clearly portable to other systems where impact pits are preserved on magma-transported solids.

478   As an illustration of the method, two olivine grains and two garnet grains from Diavik A154N

479   coherent kimberlite were carefully extracted and had their impact pits measured (Figure S4).

480   Measurements (n =16) on the two olivine grains ($k_{olivine} = 0.62$) corresponds to impact velocities in the

481   range of 2.6 – 6.0 m s^{-1} and 2.5 – 5.0 m s^{-1} (Figure 8b). Similarly, measurements (n = 11) on the two

482   garnet grains (k_{garnet} = 0.46) corresponds to impact velocities of 2.9 – 4.2 m s^{-1} and 4.0 – 6.2 m s^{-1}

483   (Figure 8c). These velocities obtained independently from olivine and garnet xenocrysts hosted in

484   coherent kimberlite show remarkable agreement. These impact velocities of ~4 m s^{-1} are in excellent

485   agreement with kimberlite dyke ascent models (e.g. Sparks et al., 2006). However, it is important to

486   note that these velocities are subject to coupling between the xenocryst and the ascending magma.

487   Furthermore, the internal flow velocity within the dyke is not necessarily the same as the dyke

488   propagation velocity (Kavanagh et al., 2018).

489

490

491
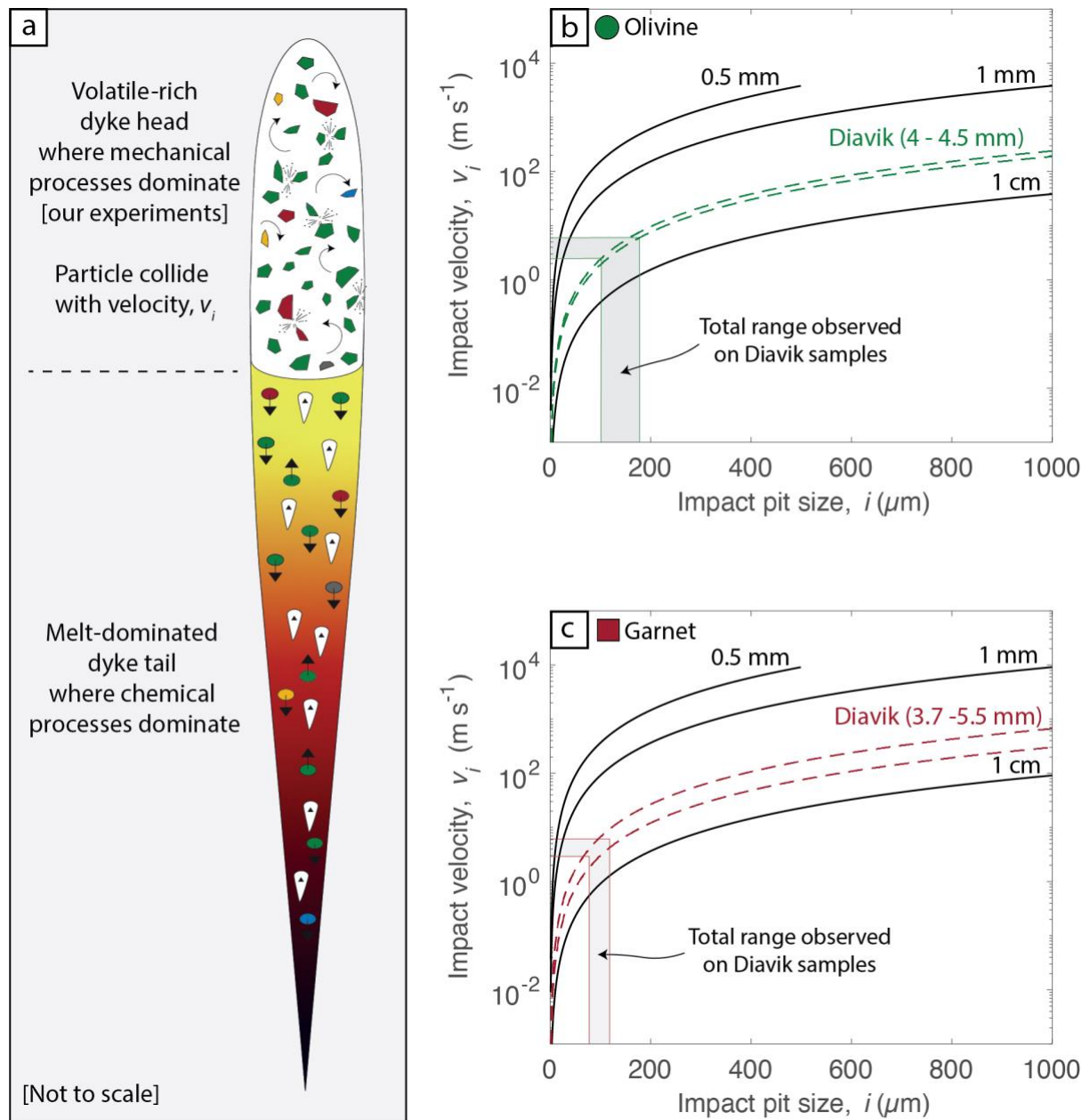
Figure 8: (a) Schematic model diagram of the ascending dyke after Brett et al., (2015) and Russell et al., (2019). Model relationships between impact velocity and pit size for different size grains of **(b)** olivine and **(c)** garnet using *k* values of 0.62 and 0.46 respectively. Pit sizes were measured for two grains of olivine and two grains of garnet from the Diavik A154N pipe are shown by the dashed curves (with the grain size listed). The total range of impact pit sizes and the corresponding, calculated impact velocities are shown by the grey shaded regions.

5. Conclusions

A diverse range of magmas erupt carrying abundant mantle xenolithic cargo in the form of xenoliths

and xenocrysts. The common xenolith-bearing magma types include alkaline basalt, basanite,

nephelinite and, especially, lamprophyre and kimberlites. These magmas sample mantle material at

503   depth from the base of the mantle lithosphere to the Moho. The successful entrainment and transport

504   of the dense mantle cargo is likely indicative of magmas fluidized by supercritical fluids or gas

505   (depending on depth) and high ascent velocities capable of turbulent flow. Where this environment is

506   sustained it creates the ideal environment for mechanical modification (i.e. attrition) of the solid

507   cargo.

508   In this study we showed that all mantle xenocrysts are susceptible to mechanical modification

509   on the timescales expected for kimberlite transport. The different mantle minerals are variably

510   susceptible to mechanical modification with olivine breaking down at the fastest rate and diamond the

511   slowest. With further study, xenocryst mass loss could be inverted to better constrain source melt

512   compositions. Lastly, we develop an empirical model to relate the impact pits observed on both our

513   experimental products and natural kimberlitic xenocrysts to the differential velocities of xenocrysts

514   during transport. Applying this concept to garnet and olivine xenocrysts extracted from samples of

515   coherent kimberlite we independently arrive at xenocryst velocities of ~4 m s^{-1}, thereby providing a

516   direct estimate of transport velocity for these enigmatic cargo-laden magmas. The concept of

517   converting impact pits preserved on magma-transported solids is clearly portable to other systems.

518

524   **References:**
525   Archard, J., 1953. Contact and rubbing of flat surfaces. J. Appl. Phys. 24, 981–988.
526   Arndt, N.T., Boullier, A.-M., Clément, J.-P., Dubois, M., Schissel, D., 2006. What olivine, the
527   neglected mineral, tells us about kimberlite petrogenesis. eEarth Discuss. 1, 37–50.
528   Arndt, N.T., Guitreau, M., Boullier, A.-M., Le Roex, A., Tommasi, A., Cordier, P., Sobolev, A., 2010.
529   Olivine, and the origin of kimberlite. J. Petrol. 51, 573–602.
530   Barton Jr, J.M., Gerya, T. V, 2003. Mylonitization and decomposition of garnet: evidence for rapid
531   deformation and entrainment of mantle garnet-harzburgite by kimberlite magma, K1 Pipe,
532   Venetia Mine, South Africa. South African J. Geol. 106, 231–242.
533   Bemrose, C.R., Bridgwater, J., 1987. A review of attrition and attrition test methods. Powder Technol.
534   49, 97–126.
535   Bi, H.T., Grace, J.R., 1995. Flow regime diagrams for gas-solid fluidization and upward transport. Int.
536   J. Multiph. Flow 21, 1229–1236.
537   Boerefijn, R., Ghadiri, M., Salatino, P., 2007. Attrition in fluidised beds. Handb. Powder Technol. 12,
538   1019–1053.
539   Bonfils, B., Ballantyne, G.R., Powell, M.S., 2016. Developments in incremental rock breakage testing
540   methodologies and modelling. Int. J. Miner. Process. 152, 16–25.

541   Brett, R.C., Russell, J.K., Andrews, G.D.M., Jones, T.J., 2015. The ascent of kimberlite: Insights from
542   olivine. Earth Planet. Sci. Lett. 424, 119–131. https://doi.org/10.1016/j.epsl.2015.05.024
543   Brown, R.J., Manya, S., Buisman, I., Fontana, G., Field, M., Mac Niocaill, C., Sparks, R.S.J., Stuart,
544   F.M., 2012. Eruption of kimberlite magmas: physical volcanology, geomorphology and age of
545   the youngest kimberlitic volcanoes known on earth (the Upper Pleistocene/Holocene Igwisi
546   Hills volcanoes, Tanzania). Bull. Volcanol. 74, 1621–1643.
547   Brown, R.J., Valentine, G.A., 2013. Physical characteristics of kimberlite and basaltic intraplate
548   volcanism and implications of a biased kimberlite record. Bulletin 125, 1224–1238.
549   Campbell, M.E., Russell, J.K., Porritt, L.A., 2013. Thermomechanical milling of accessory lithics in
550   volcanic conduits. Earth Planet. Sci. Lett. 377, 276–286.
551   Dawson, J.B., 1971. Advances in kimberlite geology. Earth-Science Rev. 7, 187–214.
552   Dufek, J., Manga, M., Patel, A., 2012. Granular disruption during explosive volcanic eruptions. Nat.
553   Geosci. 5, 561–564.
554   Eggler, D.H., 1989. Kimberlites: how do they form. Kimberlites Relat. rocks 1, 489–504.
555   Fedortchouk, Y., 2019. A new approach to understanding diamond surface features based on a review
556   of experimental and natural diamond studies. Earth-science Rev.
557   Ghadiri, M., Zhang, Z., 2002. Impact attrition of particulate solids. Part 1: A theoretical model of
558   chipping. Chem. Eng. Sci. 57, 3659–3669.
559   Giuliani, A., 2018. Insights into kimberlite petrogenesis and mantle metasomatism from a review of
560   the compositional zoning of olivine in kimberlites worldwide. Lithos 312–313, 322–342.
561   Gwyn, J.E., 1969. On the particle size distribution function and the attrition of cracking catalysts.
562   AIChE J. 15, 35–39.
563   Hutchings, I.M., 1993. Mechanisms of wear in powder technology: a review. Powder Technol. 76, 3–
564   13.
565   Jones, T.J., McNamara, K., Eychenne, J., Rust, A.C., Cashman, K. V., Scheu, B., Edwards, R., 2016.
566   Primary and secondary fragmentation of crystal bearing intermediate magma. J. Volcanol.
567   Geotherm. Res. 327, 70–83. https://doi.org/10.1016/j.jvolgeores.2016.06.022
568   Jones, T.J., Russell, J.K., 2018. Attrition in the kimberlite system. Mineral. Petrol. 1–11.
569   https://doi.org/10.1007/s00710-018-0580-0
570   Jones, T.J., Russell, J.K., 2017. Ash production by attrition in volcanic conduits and plumes. Sci. Rep.
571   7, 5538. https://doi.org/10.1038/s41598-017-05450-6
572   Jones, T.J., Russell, J.K., Lim, C.J., Ellis, N., Grace, J.R., 2017. Pumice attrition in an air-jet. Powder
573   Technol. 308, 298–305. https://doi.org/10.1016/j.powtec.2016.11.051
574   Jones, T.J., Russell, J.K., Porritt, L.A., Brown, R.J., 2014. Morphology and surface features of olivine
575   in kimberlite: implications for ascent processes. Solid Earth 5, 313. https://doi.org/10.5194/se-5-
576   313-2014
577   Jones, T.J., Russell, J.K., Sasse, D., 2019. Modification of mantle cargo by turbulent ascent of
578   kimberlite. Front. Earth Sci. 7, 134. https://doi.org/10.3389/feart.2019.00134
579   Kamenetsky, V.S., Kamenetsky, M.B., Sobolev, A. V, Golovin, A. V, Demouchy, S., Faure, K.,
580   Sharygin, V. V, Kuzmin, D. V, 2008. Olivine in the Udachnaya-East kimberlite (Yakutia,
581   Russia): types, compositions and origins. J. Petrol. 49, 823–839.
582   Kavanagh, J.L., Burns, A.J., Hazim, S.H., Wood, E.P., Martin, S.A., Hignett, S., Dennis, D.J.C., 2018.
583   Challenging dyke ascent models using novel laboratory experiments: implications for
584   reinterpreting evidence of magma ascent and volcanism. J. Volcanol. Geotherm. Res. 354, 87–
585   101.
586   Kavanagh, J.L., Sparks, R.S.J., 2009. Temperature changes in ascending kimberlite magma. Earth
587   Planet. Sci. Lett. 286, 404–413.
588   King, R.P., 2001. Modeling and simulation of mineral processing systems. Elsevier.
589   Knight, A., Ellis, N., Grace, J.R., Lim, C.J., 2014. CO 2 sorbent attrition testing for fluidized bed
590   systems. Powder Technol. 266, 412–423.
591   Kueppers, U., Putz, C., Spieler, O., Dingwell, D.B., 2012. Abrasion in pyroclastic density currents:
592   insights from tumbling experiments. Phys. Chem. Earth, Parts A/B/C 45, 33–39.
593   Kurszlaukis, S., Barnett, W.P., 2003. Volcanological and Structural Aspects of the Venetia Kimberlite
594   Cluster--a case study of South African kimberlite maar-diatreme volcanoes. South African J.
595   Geol. 106, 165–192.

596 Little, L., Mainza, A.N., Becker, M., Wiese, J., 2017. Fine grinding: How mill type affects particle
597   shape characteristics and mineral liberation. Miner. Eng. 111, 148–157.
598 Mader, H.M., Llewellin, E.W., Mueller, S.P., 2013. The rheology of two-phase magmas: A review
599   and analysis. J. Volcanol. Geotherm. Res. 257, 135–158.
600 Manga, M., Patel, A., Dufek, J., 2011. Rounding of pumice clasts during transport: field
601   measurements and laboratory studies. Bull. Volcanol. 73, 321–333.
602 McGetchin, T.R., Nikhanj, Y.S., Chodos, A.A., 1973. Carbonatite-kimberlite relations in the Cane
603   Valley Diatreme, San Juan County, Utah. J. Geophys. Res. 78, 1854–1869.
604 Mitchell, R.H., 1986. Kimberlites: petrology, mineralogy and geochemistry, 1st ed. Springer Science
605   & Business Media. https://doi.org/10.1007/978-1-4899-0568-0
606 Mitchell, R.H., Giuliani, A., O'Brien, H., 2019. What is a kimberlite? Petrology and mineralogy of
607   hypabyssal kimberlites. Elem. An Int. Mag. Mineral. Geochemistry, Petrol. 15, 381–386.
608 Moss, S., Russell, J.K., Smith, B.H.S., Brett, R.C., 2010. Olivine crystal size distributions in
609   kimberlite. Am. Mineral. 95, 527–536.
610 Peltonen, P., Kinnunen, K.A., Huhma, H., 2002. Petrology of two diamondiferous eclogite xenoliths
611   from the Lahtojoki kimberlite pipe, eastern Finland. Lithos 63, 151–164.
612 Peterson, T.D., LeCheminant, A.N., 1993. Glimmerite xenoliths in Early Proterozoic ultrapotassic
613   rocks from the Churchill Province. Can. Mineral. 31, 801–819.
614 Pilbeam, L.H., Nielsen, T.F.D., Waight, T.E., 2013. Digestion fractional crystallization (DFC): an
615   important process in the genesis of kimberlites. Evidence from olivine in the Majuagaa
616   kimberlite, southern West Greenland. J. Petrol. 54, 1399–1425.
617 Russell, J.K., Porritt, L.A., Lavallée, Y., Dingwell, D.B., 2012. Kimberlite ascent by assimilation-
618   fuelled buoyancy. Nature 481, 352–356.
619 Russell, J.K., Sparks, R.S.J., Kavanagh, J.L., 2019. Kimberlite Volcanology: Transport, Ascent, and
620   Eruption. Elem. An Int. Mag. Mineral. Geochemistry, Petrol. 15, 405–410.
621 Smith, B.H.S., 2008. Canadian kimberlites: geological characteristics relevant to emplacement. J.
622   Volcanol. Geotherm. Res. 174, 9–19.
623 Smith, D., Griffin, W.L., 2005. Garnetite xenoliths and mantle--water interactions below the Colorado
624   Plateau, southwestern United States. J. Petrol. 46, 1901–1924.
625 Sparks, R.S.J., 2013. Kimberlite volcanism. Annu. Rev. Earth Planet. Sci. 41, 497–528.
626 Sparks, R.S.J., Baker, L., Brown, R.J., Field, M., Schumacher, J., Stripp, G., Walters, A., 2006.
627   Dynamical constraints on kimberlite volcanism. J. Volcanol. Geotherm. Res. 155, 18–48.
628 Weit, A., Roche, O., Dubois, T., Manga, M., 2018. Experimental measurement of the solid particle
629   concentration in geophysical turbulent gas-particle mixtures. J. Geophys. Res. Solid Earth 123,
630   3747–3761.
631 Wilson, L., Head, J.W., 2007. An integrated model of kimberlite ascent and eruption. Nature 447, 53–
632   57.
633 Win, T.T., Davies, R.M., Griffin, W.L., Wathanakul, P., French, D.H., 2001. Distribution and
634   characteristics of diamonds from Myanmar. J. Asian Earth Sci. 19, 563–577.
635 Zhang, Z., Ghadiri, M., 2002. Impact attrition of particulate solids. Part 2: Experimental work. Chem.
636   Eng. Sci. 57, 3671–3686.
637